Experimental and numerical investigation on mixing and axial dispersion in Taylor–Couette flow patterns

Marouan Nemri[a,b], *Eric Climent*[b], *Sophie Charton*[a,*], *Jean-Yves Lanoë*[a], *Denis Ode*[a]

[a] *CEA, DEN, DTEC, SGCS, F-30207, Bagnols-sur-Cèze, France*
[b] *Institut de Mécanique des Fluides de Toulouse – CNRS – INP – UPS, Allée du Pr. Camille Soula, 31400 Toulouse, France*

A B S T R A C T

Taylor–Couette flows between two concentric cylinders have great potential applications in chemical engineering. They are particularly convenient for two-phase small scale devices enabling solvent extraction operations. An experimental device was designed with this idea in mind. It consists of two concentric cylinders with the inner one rotating and the outer one fixed. Moreover, a pressure driven axial flow can be superimposed. Taylor–Couette flow is known to evolve towards turbulence through a sequence of successive hydrodynamic instabilities. Mixing characterized by an axial dispersion coefficient is extremely sensitive to these flow bifurcations, which may lead to flawed modelling of the coupling between flow and mass transfer. This particular point has been studied using experimental and numerical approaches. Direct numerical simulations (DNS) of the flow have been carried out. The effective diffusion coefficient was estimated using particles tracking in the different Taylor–Couette regimes. Simulation results have been compared with literature data and also with our own experimental results. The experimental study first consists in visualizing the vortices with a small amount of particles (Kalliroscope) added to the fluid. Tracer residence time distribution (RTD) is used to determine dispersion coefficients. Both numerical and experimental results show a significant effect of the flow structure on the axial dispersion.

Keywords: Taylor–Couette flow; Axial dispersion; Direct numerical simulation; Experiments

1. Introduction

Annular centrifugal contactors based on Taylor–Couette flow geometry have a great potential in chemistry, metallurgy and, since the prior works of Davies and Weber (1960), in the nuclear industry where they are particularly suitable for small-scale studies of solvent extraction processes.

Since the work of Taylor (1923), Taylor–Couette flow has been extensively studied due to its nonlinear dynamics. It is a widely studied flow, known to evolve towards turbulence through a sequence of successive instabilities as the inner cylinder rotation rate increases.

Beyond a critical speed of the rotating cylinder, pure azimuthal Couette flow results in the formation of toroidal vortices, called Taylor vortex flow (TVF). This critical condition is expressed by the Taylor number (*Ta*) or equivalently by the Reynolds number (*Re*) based on the gap width e, the inner cylinder linear velocity ΩR_i and the fluid viscosity ν. At higher Reynolds numbers a secondary instability causes the flow to become time-dependent due to the appearance of an azimuthal wave (deformation of the vortices). This flow state, known as wavy vortex flow (WVF), is characterized by: an axial wave number n (or alternatively a mean axial wavelength λ) and an azimuthal wave number noted m. As *Re* further increases, the wavy flow becomes increasingly modulated by additional frequencies (MWVF) and eventually becomes turbulent.

These flow instabilities have been the topic of many studies (Coles, 1965; Fenstermacher et al., 1979). Such flow patterns provide high values of heat and mass transfer coefficients, which explains why some important industrial operations (emulsion polymerization, heterogeneous catalytic

* *Corresponding author.*
E-mail address: sophie.charton@cea.fr (S. Charton).

http://dx.doi.org/10.1016/j.cherd.2012.11.010

Nomenclature

Notation

D_x	dispersion coefficient ($cm^2\ s^{-1}$)
D_x^*	effective dispersion coefficient
e	gap width
f	temporal dominant frequency of the travelling wave (s^{-1})
f'	frequency of modulation (s^{-1})
G	normalized torque
H	annulus height
m	azimuthal wave number
n	axial wave number
R_e	outer cylinder radius
$Re = (\Omega R_i e)/\nu$	Reynolds number
$Re_{ax} = (u_x e)/\nu$	axial Reynolds number
Re_c	critical Reynolds number
R_i	inner cylinder radius
$Sc = \nu/D_x$	dispersion based Schmidt number
T_c	duration of a rotor complete rotation (s)
$Ta = Re\sqrt{e/R_i}$	Taylor number
V_φ	angular speed of travelling wave ($rad\ s^{-1}$)
Ω	rotational rate for the rotor
η	radius ratio (R_i/R_e)
Γ	aspect ratio (H/e)
λ	axial wavelength
ρ_f	density ($kg\ m^{-3}$)
μ	dynamic viscosity ($Pa\ s^{-1}$)
ν	kinematic viscosity ($m^2\ s^{-1}$)
DNS	direct numerical simulation
MWVF	modulated wavy vortex flow
PIV	particle image velocimetry
RTD	residence time distribution
TVF	Taylor vortex flow
WVF	wavy vortex flow

reactions, and liquid–liquid extraction) can take advantage of Taylor–Vortex equipment.

When a weak axial flow is superimposed upon Taylor–Couette flow (PTC, Poiseuille Taylor Couette), axial motion of the Taylor vortices transports the cellular vortices wherein toroidal motion of fluid elements yields efficient mixing. Such a flow system can be considered as a near-ideal plug-flow reactor (PFR). Many researchers have investigated the axial dispersion in Taylor–Couette flows (Tam and Swinney, 1987; Moore and Cooney, 1995; Desmet et al., 1996; Campero and Vigil, 1997; Ohmura et al., 1997; Rudman, 1998). Experimental observations referenced in the literature (Tam and Swinney, 1987; Ohmura et al., 1997) indicate that axial dispersion decreases to a minimum near the onset of Taylor vortices and increases further as the Taylor number (Ta) increases.

The present study was carried out in the general context of the application of Taylor–Couette flow for liquid–liquid extraction and particularly for the extraction of nuclear waste (uranium, plutonium) from spent nuclear fuels. We focus on the mixing properties of the single phase flow. The flow bifurcations as well as the axial dispersion in the Taylor–Couette apparatus were studied using both experimental and numerical approaches.

Table 1 – Apparatus geometry and operating conditions.

Parameters	First prototype	Second prototype
Rotor radius (R_i)	8.5 mm	24 mm
Shaft radius (R_e)	10 mm	35 mm
Gap width	1.5 mm	11 mm
Radius ratio (η)	0.85	0.68
Length (H)	720 mm	640 mm
Aspect ratio (Γ)	480	58
Rotation speed	80–1600 rpm	4–1000 rpm
Re range (water)	107–2136	111–27,646

2. Methodology

2.1. *Experimental methods*

2.1.1. *Description of the apparatus*

The device consists of two concentric cylinders with the inner cylinder rotating (the outer cylinder is fixed) and with the possibility of superimposing a pressure driven-flow in the axial direction. Two geometrical configurations are used in this study (Table 1).

- The first one was designed to study the mixing performances with a minimum volume of fluid. This first device is therefore characterized by a small gap width $e = 1.5$ mm.
- The second prototype, with a larger gap width, $e = 11$ mm, was designed for specific optical investigations (PIV, PLIF).

The main features of the experimental device are shown in Fig. 1.

As the flow state is strongly dependent on the flow history, a speed control system was used. A ramp generator controls the rotor acceleration during transient evolution to the desired

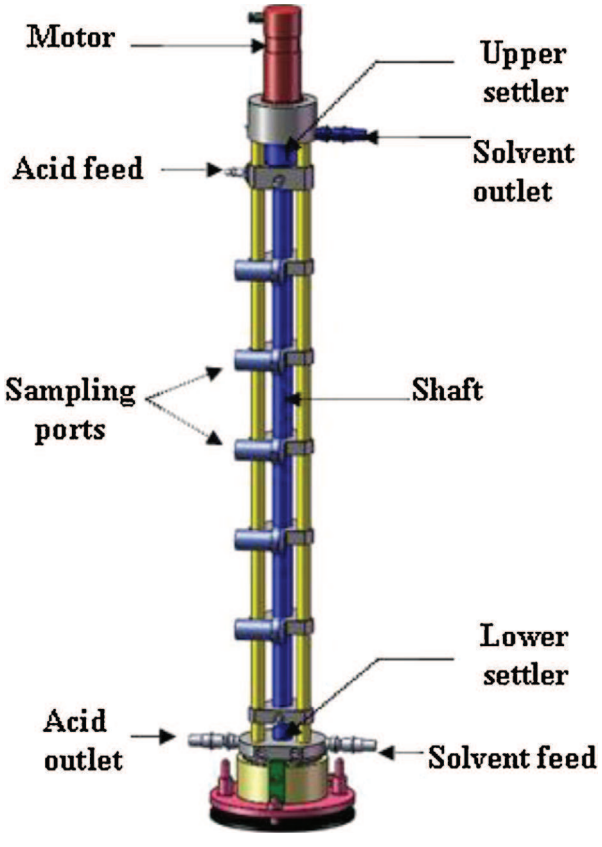

Fig. 1 – Schematic presentation of the apparatus ($\eta = 0.85$).

Table 2 – Fluids properties for "visualization" and RTD experiments.

Fluid	Density ($kg\,m^{-3}$)	Viscosity (Pa s)
Kalliroscope solution	1000	1.4×10^{-3}
Nitric acid 0.5 N	1018	9.7×10^{-4}
Solvent (TBP 30% in TPH)	826	1.5×10^{-3}

Reynolds number. Indeed, for the same Reynolds number, *Re*, and using different acceleration ramps provides various flow states. Therefore, a given wave state is established by following a prescribed start-up protocol, as determined by the flow visualization technique (see Section 2.2.1). This procedure ensures reproducibility of the measurements.

2.1.2. *Measurement techniques*

The flow pattern was visualized using an aqueous solution seeded with Kalliroscope AQ-1000 flakes. These particles consist of small, light reflecting slabs which align themselves along streamlines. Using a high-speed camera, the different transitions can be visualized. In order to fully characterize the different wavy regimes, a spectral analysis of the data was performed to determine the wave state (axial and azimuthal wave numbers).

Axial dispersion in single phase flow was investigated with two different liquids: an organic phase (TBP 30% in TPH) and an aqueous phase (0.5 N, HNO_3). The fluids properties are summarized in Table 2. Tracer experiments were performed by placing optical sensors at the top and bottom of the column. The annular cavity was then filled with the appropriate fluid and the tracer (methylene blue or Sudan red) was injected through a specific orifice. The coloured tracer dispersion was monitored online with a spectrometer mounted onto a CCD sensor. All experimental conditions were set to be within the linear range of the Beer–Lambert law (tracer concentration is proportional to its absorbance). Once normalized, the curve of absorbance gives direct access to the residence time distribution (RTD).

Most models of axial mixing in single-phase Taylor–Couette flow are based on a diffusion equation. Alternatively, stirred tanks in series can model tracer response curves. Both modelling approaches can be used to determine the effective axial dispersion coefficients by matching model prediction to experimental results (Tam and Swinney, 1987). However, even for single-phase systems, simple models are not always suitable, especially at Taylor numbers below the onset of turbulent Taylor vortex flow (Desmet et al., 1996; Campero and Vigil, 1997). In this paper, mathematical models based on species mass balances applied to a near-ideal plug-flow reactor are used. Numerical fitting between experimental tracer response curves (RTD) and mathematical models lead to a dispersion coefficient estimate (see Fig. 2).

2.2. *Numerical methods*

2.2.1. *Direct numerical simulations of the carrying flow*

In the present study, direct numerical simulations (DNS) was carried out with the JADIM finite volume code developed at IMFT.

The fluid is considered incompressible and Newtonian with constant physical properties. The governing Navier–Stokes equations are then written:

$$\nabla \cdot \mathbf{u} = 0 \tag{1}$$

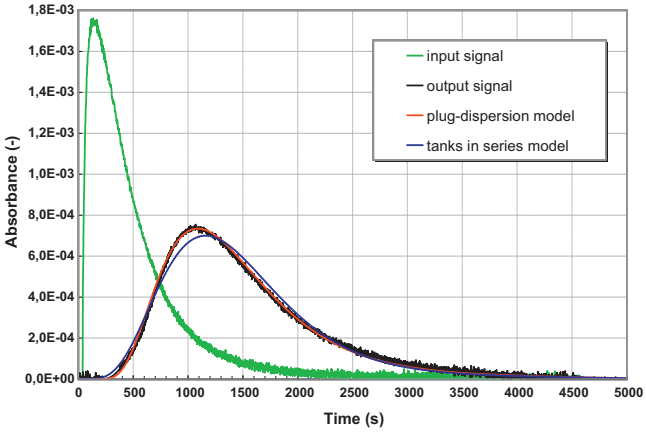

Fig. 2 – Dye tracer experiments: input (green) and output (black) signals and output signals model by either plug flow with axial dispersion model (red) or tanks in series model (blue). (For interpretation of the references to colour in this figure legend, the reader is referred to the web version of the article.)

$$\rho_f \left(\frac{\partial \mathbf{u}}{\partial t} + \mathbf{u} \cdot \nabla \mathbf{u} \right) = -\nabla P + \nabla . \left[\mu \left(\nabla \mathbf{u} + \nabla^T \mathbf{u} \right) \right] \tag{2}$$

where ρ_f is the fluid density and μ the dynamic viscosity.

The Navier–Stokes equations were solved using a velocity–pressure formulation (2) and were discretized on a staggered non-uniform grid, using a centred second-order scheme. The time integration was achieved through a third-order Runge–Kutta scheme and a second-order implicit Crank–Nicolson scheme for the viscous terms.

The geometry is described in Fig. 3. The radius ratio is $\eta = R_i/R_e$, the height of the numerical domain is $L = 3\lambda$ (where the axial wavelength is correlated with the gap width from $\lambda = 2e$ to $\lambda = 2.29e$ depending on the *Re* value) so three axial wavelengths were simulated. Periodic boundary conditions were used in the axial direction. Finally, the domain length

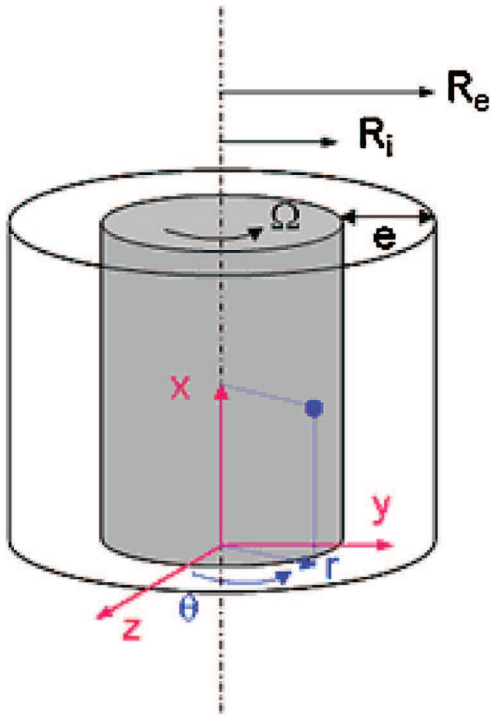

Fig. 3 – Computational domain.

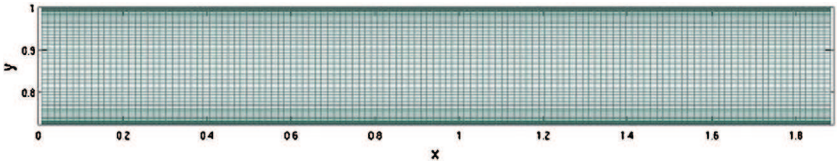

Fig. 4 – Mesh grid (plane *xy*).

L was varied in order to study the influence of the axial wavelength λ.

All simulations were carried out using dimensionless units. All flow-related quantities were scaled using the outer cylinder radius R_e and the reference velocity ΩR_i where Ω is the rotation rate of the inner cylinder. This yields $R_i = \eta$, $R_e = 1$ and $\Omega R_i = 1$. A uniform mesh was used in the axial and azimuthal directions. The grid was stretched in the radial direction to better describe the boundary layers near the walls (Fig. 4).

To quantify axial dispersion, the method proposed by Rudman (1998) was applied. An "effective particle diffusion coefficient", based on the chaotic advection of a large number of fluid particles, was derived from Lagrangian transient simulations. An axial dispersion coefficient was defined by Eq. (3). Those particles were advected by the carrying fluid flow. Transport within vortices supplemented by inter-vortex mixing resulted in enhanced axial dispersion.

$$D_x^* = \lim_{t\to\infty} D_x^*(t) = \lim_{t\to\infty}\left\{\frac{1}{N}\sum_i \frac{\left\langle (x_i(t) - x_i(0))^2\right\rangle}{2t}\right\} \quad (3)$$

In Eq. (3) $x_i(t)$ is the axial position of the ith particle at time step t, $x_i(0)$ its initial position (both x and t are dimensionless) and N the total number of particles seeded in the flow.

A large number of particles (1000–10,000) are randomly seeded throughout the computational domain, and their trajectories are tracked over time. The instantaneous value of D_x^* increases with time until it reaches a plateau value indicative of long-time diffusive axial mixing (Fig. 5). The dimensional (or "effective") dispersion coefficient, D_x is obtained by: $D_x = (\nu Re D_x^*)/(1-\eta)$. Mixing property can be compared with momentum diffusion through the dispersion based Schmidt number defined as $Sc = \nu/D_x$.

Particles trajectories illustrate the different transport mechanisms: within vortex or between neighbouring vortices (see Fig. 6). Intra-vortex mixing is due to the chaotic

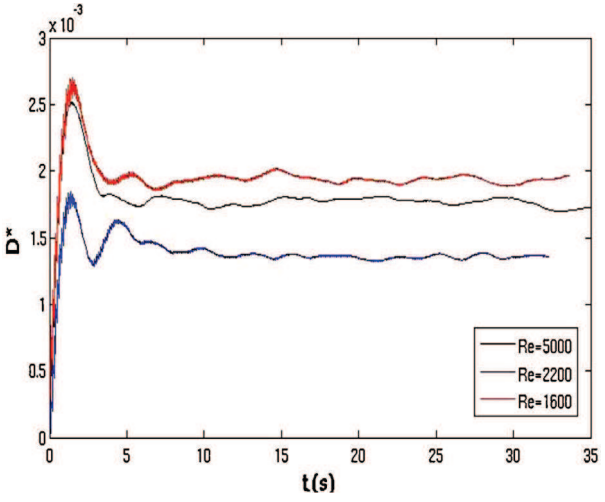

Fig. 5 – Effective dispersion coefficient evolution with time.

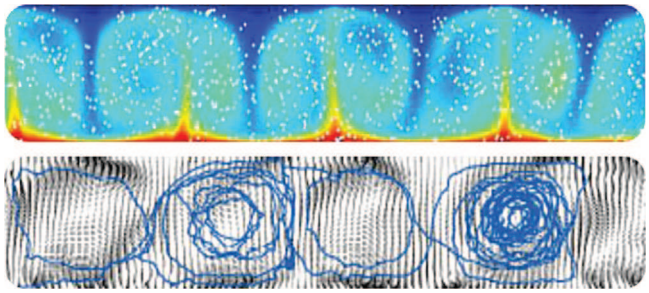

Fig. 6 – Particles positions in the computational domain (top). Example of a particle path (bottom).

particle paths induced by the three-dimensional velocity fields. Inter-vortex transport occurs when the waves induces fluid exchange through neighbouring vortices. The combination of these two mechanisms results in enhanced axial dispersion.

2.2.2. *Note on axial flow-rate effect*

RTD measurements are carried out with a weak axial Poiseuille flow. In Fig. 7, it is clear that the axial dispersion coefficient is only weakly influenced in this range of axial mean flow rate. Moreover, we have carried out several simulations with and without axial flow of the same magnitude as in experiments. Since no significant deviation of the flow patterns was observed for a flow rate Q_{ax} lower than 300 ml h^{-1}, the effect of axial flow was assumed to be negligible. The axial flow is not taken into account for the numerical simulations coupled to Lagrangian particle tracking.

3. Results and discussion

3.1. *Flow characteristics from experiments*

The different flow regimes have been identified by an experimental visualization technique described in Section 2.1.2. For the two configurations studied ($e = 1.5$ mm and $e = 11$ mm) all flow transitions were identified. Fig. 8 shows the visualization

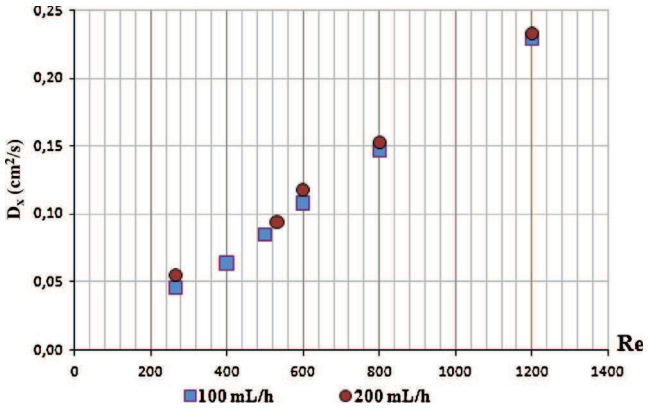

Fig. 7 – Evolution of the dispersion coefficient as a function of *Re* for different axial flow rate Q_{ax} ($\eta = 0.85$).

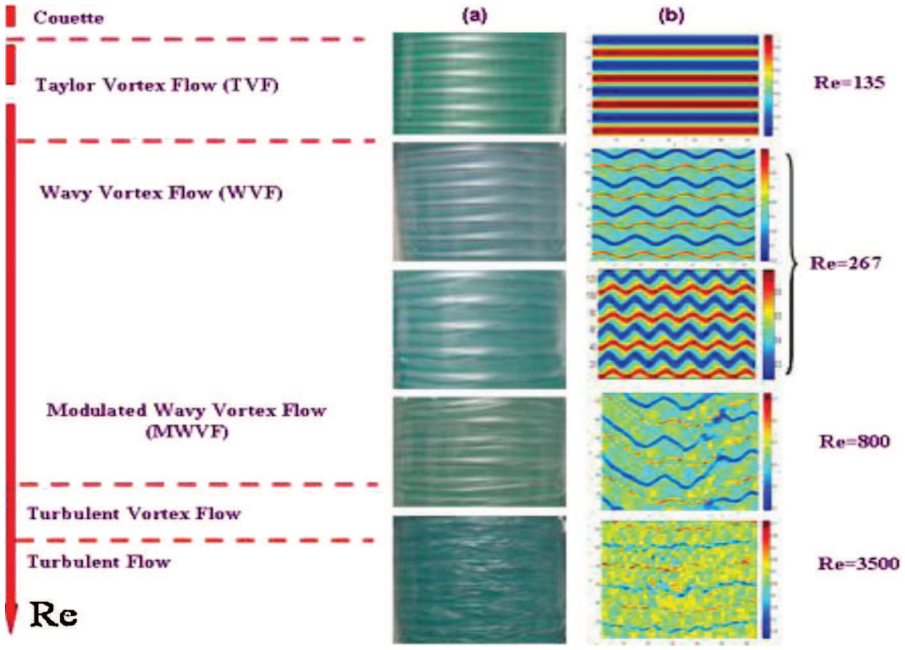

Fig. 8 – Illustration of different flow regimes ($\eta = 0.85$). (a) Visualization of experiments and (b) numerical simulations.

Table 3 – Summary of the flow characteristics for device geometry #1 ($\eta = 0.85$).

Flow regimes	*Re* of transition	Flow characteristics
Taylor vortex flow (TVF)	$Re_c = 125$	$\lambda = 2.01e$
Wavy vortex flow (WVF)	$1.32Re_c < Re < 5.44Re_c$	$\lambda = 2.19e$ to $2.61e$, $m = 2$ to 8
Modulated wavy vortex flow (WVF)	$5.44Re_c < Re < 9.2Re_c$	$\lambda = 2.63e$ to $3.1e$, $m = 4$ to 7
Turbulent flow	$Re > 9.2Re_c$	$\lambda > 3.1e$

of the flow structure at five different *Re* numbers. The first flow bifurcation (TVF) occurred near $Re_c = 125$ for the geometry $\eta = 0.85$. This value is in agreement with transition point predicted by Rudman (1998) and Coles (1965) of $Re_c = 119$. For the second geometry $\eta = 0.68$, the transition Reynolds number Re_c was estimated at 79 which is also in agreement with the literature (Takeda et al., 1990). The WVF regime was observed for *Re* larger than $1.32Re_c$ and $4.9Re_c$ respectively for the first and second configuration. All the characteristic of further flow transitions are summarized in Tables 3 and 4. In order to fully characterize the different wavy regimes, a spectral analysis of the image sequences is achieved. Space–time plots were generated by extracting single lines of pixel intensity at a particular spatial location. Then 2D fast Fourier transforms (FFT) of the resulting space time plots were performed. Characteristic frequency of the travelling wave (denoted f) is extracted from the temporal power spectrum. In fact, the formation of wavy vortex flow yields a well-identified temporal frequency and its harmonics. Fig. 9(b) shows the power spectrum corresponding to travelling wave at $Re = 1192$. The most energetic frequency peak corresponds to f. For wavy regimes space–time diagrams give access to the angular velocity (phase speed) of the travelling wave noted V_φ. It corresponds to the slope of the curves seen on space–time diagrams (see Fig. 9(e)). Knowing the temporal frequency f and the angular speed of the travelling wave V_φ the azimuthal wave number m based on $m = 2\pi f/V_\varphi$ was determined.

As *Re* is increased further, a modulation of the wave shape, initially perfectly periodic, appears and the flow becomes more complex. The amplitude of the rotating wave varies periodically while a modulation of the wave amplitude can be observed (Takeda et al., 1992). This corresponds to the modulated wavy vortex flow (MWVF). The dominant temporal frequency is modulated with a lower additional frequency f'.

The turbulent flow regime begins with the onset of chaotic structures that have multiple distinct frequencies around the modulation frequency f'. This initial phase is sometimes designated as "weakly turbulent regime". The regime "highly turbulent" is characterized by a broad band spectrum related to the presence of turbulent structures, without emergence of a dominant frequency.

Table 4 – Summary of the flow characteristics for device geometry #2 ($\eta = 0.68$).

Flow regimes	*Re* of transition	Flow characteristics
Taylor vortex flow (TVF)	$Re_c = 79$	$\lambda = 2.01e$
Wavy vortex flow (WVF)	$4.9Re_c < Re < 22.7Re_c$	$\lambda = 2.21e$ to $2.33e$, $m = 2$ to 7
Modulated wavy vortex flow (WVF)	$22.7Re_c < Re < 27Re_c$	$\lambda = 2.33e$ to $3.3e$, $m = 3$ to 9
Turbulent flow	$Re > 27Re_c$	$\lambda > 3.01e$

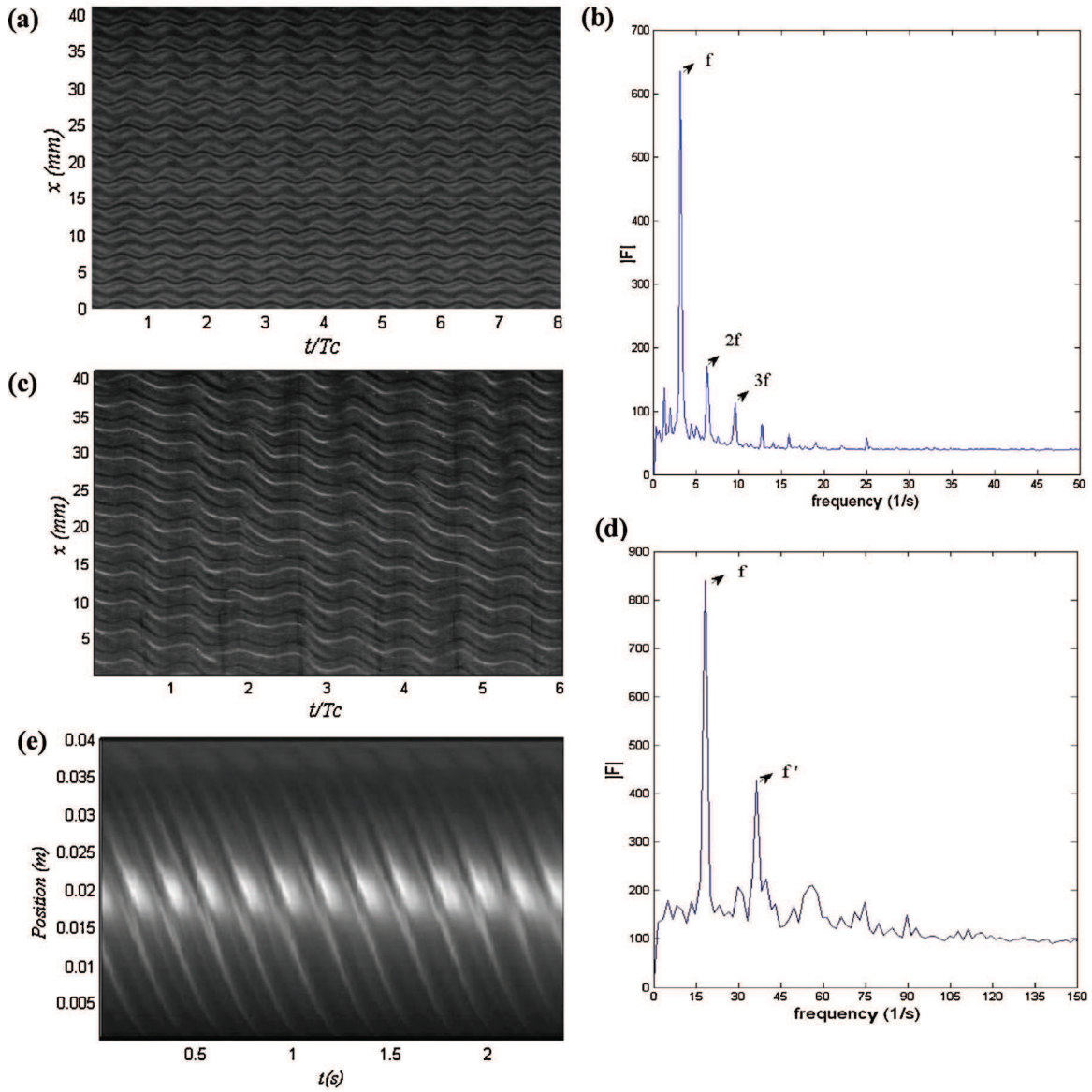

Fig. 9 – Time–space diagrams/spectrum. (a) Time history of the travelling wave at *Re* = 200 (WVF). (b) Spectrum of the travelling wave at *Re* = 200 (WVF). (c) Time history of the travelling wave at *Re* = 800 (MWVF). (d) Spectrum of the travelling wave at *Re* = 800 (MWVF). (e) Time–space diagrams *Re* = 200.

3.2. *Validation of numerical simulations*

The different regimes identified experimentally were reproduced numerically. Based on the velocity profiles obtained in DNS, the normalized viscous torque was calculated (Eq. (4)).

$$G = \frac{2\pi R_i \tau_\omega}{\rho \nu^2} \tag{4}$$

τ_ω is the viscous shear stress on the inner cylinder. Fig. 10 reports the evolution of *G* with the Reynolds number *Re*. The computed values are in good agreement with the empirical correlation proposed by Wendt (1933).

Fig. 11 shows typical snapshots of instantaneous velocity fields in the vertical plane, from top to bottom at Reynolds numbers of 140, 200 and 800. The occurrence of inter-vortex fluid transfer is strongly related to the transition to the wavy vortex flow, whereas in TVF regime vortices are essentially cellular. The vortex shape changes gradually as it fills up with fluid from neighbouring vortices and it shrinks as it loses fluid to its adjacent vortices. As *Re* is increased further, the vortex shape changes more rapidly and often displays dislocations when vortex pairs merge. This is clearly related to the modulation of the wave amplitude. As the *Re* increases even more, Taylor vortices become severely distorted and the large-

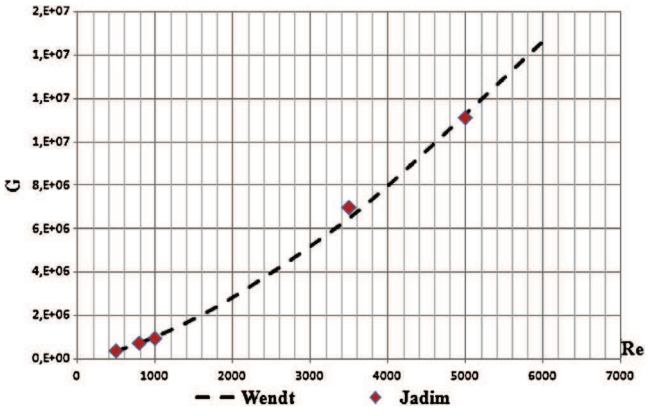

Fig. 10 – Normalized torque experienced by the inner cylinder as a function of *Re* ($\eta = 0.85$).

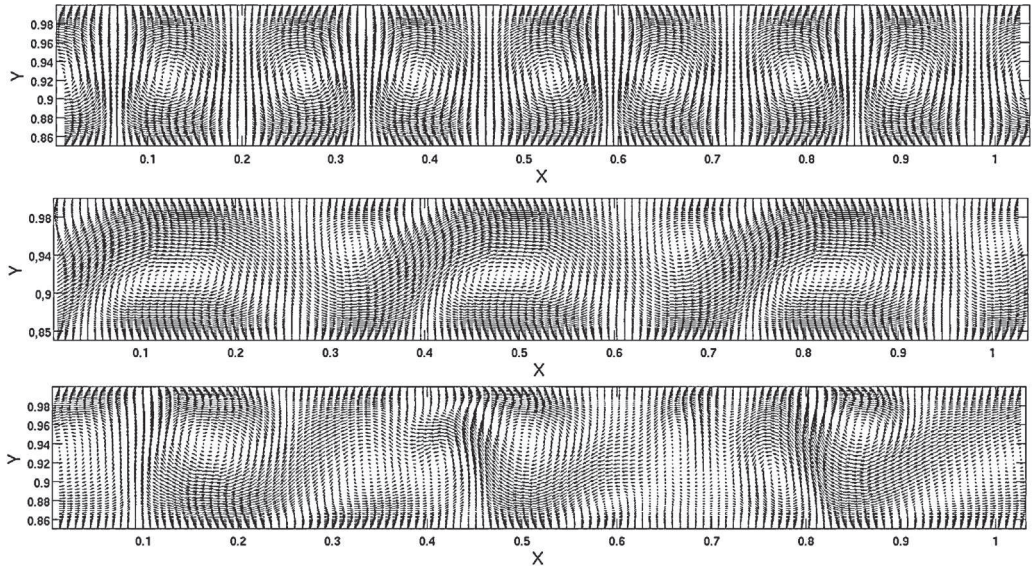

Fig. 11 – Instantaneous velocity fields on a meridian plane (*xy*) at Reynolds numbers (from top to bottom) *Re* = 140, 200 and 800 ($\eta = 0.85$).

scale vortices are contaminated with small scale structures in the wall boundary layers. This generates fluctuating energetic fluid motions.

The property of non-uniqueness has been demonstrated by the existence of hysteresis phenomena (Coles, 1965). Depending on the flow history, multiple flow states are stable for a given Reynolds number. The flow structures can be distinguished by the axial wavelength λ, ranging from 2*e* to 2.36*e* and the azimuthal wave number *m*, which range from 2 to 8. The wave number characterizes the number of wave periods over the azimuthal direction. Different wave states (λ, *m*) were observed when approaching the targeted Reynolds number *Re* with different acceleration rates of the inner cylinder rotation. Numerically, similar flow regimes are achieved by seeding the base TVF flow with weak perturbations according to the wave number *m* observed experimentally. The axial length of the domain can also be adapted to λ. The numerical results did match the experimental data very precisely. The different flow regimes are illustrated in Fig. 8.

3.3. *Axial dispersion*

In the literature, many studies suggest power laws for the evolution of the dispersion coefficient with the *Re* or *Ta* numbers (Tam and Swinney, 1987; Moore and Cooney, 1995; Ohmura et al., 1997). In these studies, the authors did not account for important flow parameters, such as the axial and the azimuthal wavelengths. Indeed, as illustrated by Fig. 12, a great variation of axial dispersion can be observed (either experimentally or numerically) for the same *Re* number. This difference is due to the non-uniqueness of the flow especially for wavy regimes. The flow state dependency is significant over the WVF and MWVF regimes while it is less obvious for turbulent flows.

While Rudman (1998) studied precisely this point only under the WVF regime, in the present work the influence of different hydrodynamic parameters (*m*, λ) on the axial dispersion coefficient has been studied over a wide range of *Re*. Using well-defined ramping protocols, along with visualization techniques guarantee the reproducibility of the flow regime, and consequently of the resulting mixing behaviour.

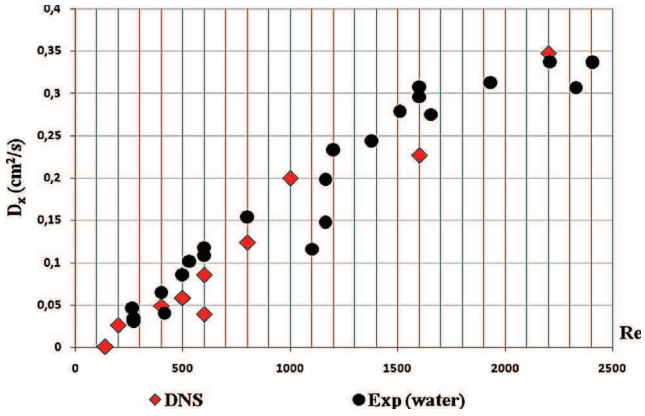

Fig. 12 – Dispersion coefficient D_x as a function of *Re* ($\eta = 0.85$).

Direct numerical simulations of the flow and Lagrangian tracking were carried out over similar flow characteristics. Good agreement between the numerical results and the experimental data was obtained, as illustrated by Figs. 12 and 13. The dispersion based Schmidt number (*Sc*) shows a general Re^{-1} trend as proposed by Moore and Cooney (1995). The transition to wavy regimes increases the dispersion coefficient dramatically: 44 enhancement factor from TVF to WVF. Actually, the wavy perturbation has two significant effects on the particle

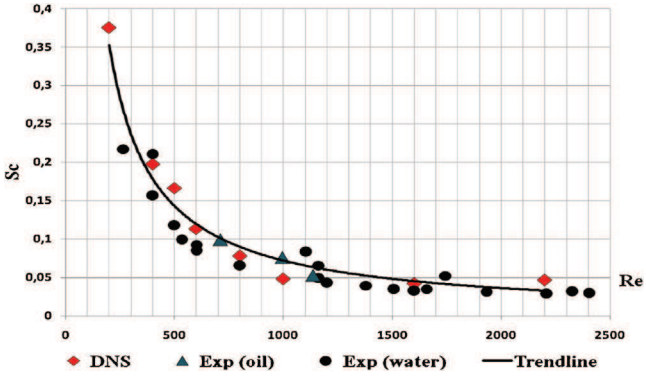

Fig. 13 – Evolution of the dispersion based Schmidt number as a function of *Re* ($\eta = 0.85$).

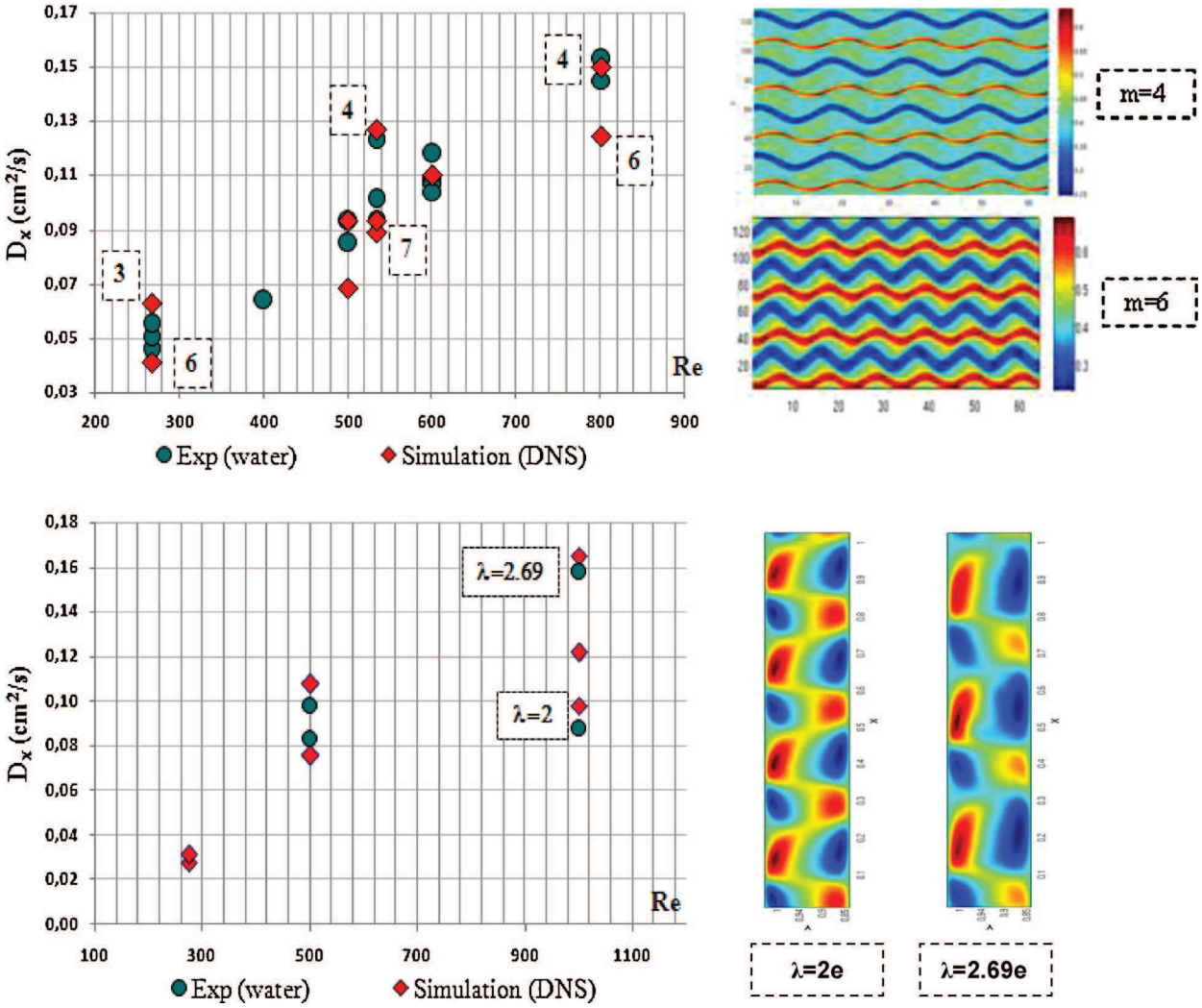

Fig. 14 – (Top) Evolution of the dispersion coefficient as a function of *Re* and azimuthal wave number *m* for $\lambda = 2.29e$. (Bottom) Evolution of the dispersion coefficient as a function of *Re* and axial wavelength λ for $m = 4$. Simulated flow patterns are shown on the right side for the sake of illustration.

motion leading to enhanced axial dispersion. First, the loss of rotational symmetry makes the velocity field dependent on all three spatial coordinates and time. This leads to chaotic particle motion and hence intravortex mixing. Second, the wavy perturbation breaks the boundary separating adjacent vortices. This provides flow streams for fluid elements to pass from one vortex to another, resulting in intervortex mixing. Rudman (1998) found that the *Sc* value reached an asymptotic value of 0.155 as *Re* increases, indicating that in wavy vortex flow beyond a certain limit of the rotation speed the axial dispersion varies very weakly. However, our results show that the modulation of the wavy flow with additional frequencies (MWVF) can influence the dispersion significantly. The dispersion based Schmidt number can go below the asymptotic value given by Rudman. This could be explained by the characteristics of this flow discussed earlier in Section 3.1. The modulation increases the interactions between vortices which enhances axial dispersion and reduces *Sc*.

The effect of the wave state on axial dispersion has also been studied. Different wave states were examined experimentally and numerically for many Reynolds numbers. The influence of both the axial and the azimuthal wave numbers is shown in Fig. 14. At first, λ was fixed and *m* was varied, then *m* was fixed and λ was varied. The dispersion coefficient D_x appears to be a decreasing function of *m*. This result is in agreement with Rudman (1998). In contrast, D_x is an increasing function of λ (Fig. 14b). This observation was confirmed by Rudman for wavy regimes and by Tam and Swinney (1987) for turbulent regimes. Tam and Swinney have proposed a correlation between D_x and λ. As a result of this significant variability, finding a relationship between D_x and the Reynolds number *Re* cannot be achieved without taking into account the wave state.

4. Conclusion

In this work, the relationship between the hydrodynamics of Taylor–Couette flow and axial dispersion of passive tracer was investigated. The influence of the successive flow bifurcations on the axial dispersion coefficient was investigated numerically as well as experimentally.

The sequence of flow instabilities has been determined using a visualization technique. Spectral analysis was used to identify transition Reynolds numbers and structural characteristics of the flow states. Direct numerical simulations of the flow were carried out as well, and all the flow-regimes were accurately reproduced. The results show how mixing is enhanced with increasing the *Re*. The structure of wavy

regimes increases the mixing within the vortices and between adjacent vortices.

The axial dispersion coefficient was numerically derived from Lagrangian tracking simulation and measured by RTD experiments. Both numerical and experimental results revealed a significant effect of the flow state on the mixing properties. Indeed, in the wavy flow regimes (WVF and MWVF) a multiplicity of stable wavy states can be achieved and D_x may vary by a factor of two for the same Reynolds number (King and Rudman, 2001). The influence of azimuthal and axial wavelengths has been investigated and a good agreement between the numerical results and experiments has also been achieved for these aspects.

References

Campero, R.J., Vigil, R.D., 1997. Axial dispersion during low Reynolds number Taylor Couette flows: intra-vortex mixing effects. Chem. Eng. Sci. 52 (19), 3303–3310.

Coles, D., 1965. Transitions in circular Couette flow. J. Fluid Mech. 21, 385–425.

Davies, M.W., Weber, E.J., 1960. Liquid–liquid extraction between rotating concentric cylinders. Ind. Eng. Chem. 52 (11), 929–934.

Desmet, G., Verelst, H., Baron, G.V., 1996. Local and global dispersion effects in Couette–Taylor flow: description and modelling of dispersion effects. Chem. Eng. Sci. 51 (8), 1287–1298.

Fenstermacher, P.R., Swinney, H.L., Gollub, J.P., 1979. Dynamical instabilities and the transition to chaotic Taylor vortex flow. J. Fluid Mech. 94, 103–128.

King, G.P., Rudman, M., 2001. Predicting chaotic dispersion with Eulerian symmetry measures: wavy Taylor-vortex flow. Phys. Fluids 13, 2522–2528.

Moore, C.M., Cooney, C.L., 1995. Axial dispersion in Taylor–Couette flow. AIChE J. 41 (3), 723–727.

Ohmura, N., Kataoka, K., Shibata, Y., Makino, T., 1997. Effective mass diffusion over cell boundaries in Taylor–Couette flow system. Chem. Eng. Sci. 52 (11), 1757–1765.

Rudman, M., 1998. Mixing and particle dispersion in the wavy vortex regime of Taylor–Couette flow. AIChE J. 44 (5), 1015–1026.

Takeda, Y., Fischer, W.E., Kobashi, K., 1990. Observation of the transient behaviour of Taylor vortex flow. Exp. Fluids 9, 103–127.

Takeda, Y., Fischer, W.E., Kobashi, K., Takada, T., 1992. Spatial characteristics of dynamic properties of modulated wavy vortex flow in a rotating Couette system. Exp. Fluids 13, 199.

Tam, W.Y., Swinney, H.L., 1987. Mass transport in turbulent Couette–Taylor flow. Phys. Rev. A 36 (3), 1374–1381.

Taylor, G.I., 1923. Stability of a viscous liquid contained between two rotating cylinders. Phil. Trans. Roy. Soc. Lond. A 223, 289–343.

Wendt, F., 1933. Turbulent flow between two rotating coaxial cylinders. Ing. Arch. 4, 577–595.